



# Photocatalysis of several organic dyes by a hierarchical $\text{Ag}_2\text{V}_4\text{O}_{11}$ micro–nanostructures

Hayder A. Abbood<sup>1,2</sup> · Kaixun Huang<sup>1</sup>

Received: 15 December 2017 / Accepted: 22 February 2018 / Published online: 23 February 2018  
© Springer Science+Business Media, LLC, part of Springer Nature 2018

## Abstract

Hierarchical  $\text{Ag}_2\text{V}_4\text{O}_{11}$  nano-protuberance-assembled submicrofibers have been successfully synthesized through a facile and surfactant-free hydrothermal strategy. Morphology and microstructures of as-fabricated products are carefully examined using TEM, SA-ED, HRTEM, FE-SEM, XPS and X-ray diffraction. A possible growth mechanism of the as-obtained  $\text{Ag}_2\text{V}_4\text{O}_{11}$  hierarchical submicrofibers is proposed by a time dependent experiments and the dosage of Ag. The as-prepared  $\text{Ag}_2\text{V}_4\text{O}_{11}$  products are further regarded as a kind of photocatalyst for the catalytic degradation of three toxic organic dyes, methyl blue (MB), methyl orange and rhodamine blue. Radical trapping experiments have been applied to confirm the photo-reaction mechanism. Compared with N-doped  $\text{TiO}_2$  and P25, the catalyst  $\text{Ag}_2\text{V}_4\text{O}_{11}$  prepared at 24 h reaction time exhibited much higher photocatalytic activity for MB degradation under visible-light illumination. It was ascribed to the formation of superoxide radicals species, and hierarchical structure. The use of ESI-MS analyses showed that the MB dye molecules were broken up by the action of the  $\text{Ag}_2\text{V}_4\text{O}_{11}$  photocatalyst, indicating the occurrence of a mineralization process. Additionally, kinetic results showed that the degradation process follows Langmuir–Hinshelwood (L–H) first-order kinetic reaction.

## 1 Introduction

The use of visible light as green energy in environmental purification is a most feasible topic in the photocatalytic technology [1, 2]. In order to minimize the impact on the water environment, the anthropogenic dyes realized after textile and chemical industries must be degraded [3, 4]. In this context, serious efforts including loading or doping with foreign species, modifying the characteristic dimensions [5], developing new multimetal oxide photocatalysis [6], are being made to enhance sunlight response of photocatalyst nanomaterials [7]. This leads to a significant alteration of

the electronic properties of these active materials and then its proportional of photoefficiency [8]. Up to now, numerous nanoscale materials, including hierarchical structure, one, two and three dimensions [9–13] have been, and continue to be, synthesized and demonstrated for improving sunlight photocatalytic activity for air cleaning and water purification [14, 15].

Over the past decades, a large number of Ag-based oxides nanostructures, such as  $\text{Ag}_2\text{O}$ ,  $\text{AgSbO}_3$  [16],  $\text{AgMO}_2$  ( $M = \text{Al}, \text{Ga}, \text{In}$ ) [17, 18]  $\text{Ag}_3\text{PO}_4$  [19, 20],  $\text{Ag}_2\text{Mo}_3\text{O}_{11}$  [21],  $\text{AgInW}_2\text{O}_8$  [22],  $\text{AgNb}(\text{Ta})\text{O}_3$  [23],  $\text{AgNb}_7\text{O}_{18}$  [24] have received a lot of attention because they have a narrow band gap ( $\leq 3.1$  eV) and excellent photocatalytic property as well as recyclability. Among these,  $\text{Ag}_2\text{V}_4\text{O}_{11}$ , indirect band gap semiconductor [25], enables versatile redox- properties dependent due to the multiple valence states of vanadium and the rich structural chemistry [26]. On the other hand, silver vanadate ( $\text{Ag}_2\text{V}_4\text{O}_{11}$ ) is employed as a widespread application as cathode material for advanced biomedical devices. Therefore,  $\text{Ag}_2\text{V}_4\text{O}_{11}$  nanoscale materials with different morphologies, such as nanobelt [27], self-coiling nanobelt [28], nanowires [29], and brush-like nanostructures [30] were synthesized by various routes. Unfortunately, little attention has been given to its other properties. Presently, Shi et al. [31] have investigated 2- propanol photodegradation

**Electronic supplementary material** The online version of this article (<https://doi.org/10.1007/s10854-018-8813-x>) contains supplementary material, which is available to authorized users.

✉ Hayder A. Abbood  
aabood2002@gmail.com

✉ Kaixun Huang  
hxxzrf@mail.hust.edu.cn

<sup>1</sup> School of Chemistry and Chemical Engineering, Huazhong University of Science and Technology, Wuhan 430074, People's Republic of China

<sup>2</sup> Department of Material Engineering, College of Engineering, Basrah University, Basra, Iraq

under visible light catalyzed by  $\text{Ag}_2\text{V}_4\text{O}_{11}$  nanotubes Wang and co-worker [32] reported the decomposition of bisphenol A by using  $\text{Ag}_2\text{V}_4\text{O}_{11}$  nanowire as a photocatalyst under visible light irradiation.

In this paper, we report the synthesis of microfiber  $\text{Ag}_2\text{V}_4\text{O}_{11}$  (Fig. 2) with nanoprotuberances through a simple hydrothermal method using vanadyl oxalate precursor with the assistance of  $\text{H}_2\text{O}_2$  and benzyl alcohol. Several influence factors, such as the concentration of silver, reaction time on final product were investigated. the formation mechanism was discussed and the photocatalytic degradation of MB, RhB, and MO of the hierarchical  $\text{Ag}_2\text{V}_4\text{O}_{11}$  was studied. The main active species were determined to be superoxide radicals under visible-light irradiation through free-radical-trapping experiments. Moreover, the photocatalytic degradation pathways and the possible intermediate products are also discussed. The result suggests as prepared  $\text{Ag}_2\text{V}_4\text{O}_{11}$  is an efficient catalyst for photocatalytic degradation of MB, compared with Degussa-P25  $\text{TiO}_2$  and N- $\text{TiO}_2$  under visible light irradiation.

## 2 Experimental

### 2.1 Materials

Ammonium metavanadate, Analytical grade tetrabutyl orthotitanate ( $\text{C}_{16}\text{H}_{36}\text{O}_4\text{Ti} > 97\%$ ), silver nitrate, vanadium pentoxide were purchased from Shanghai. Ethylenediamine, Oxalic acid dehydrates and benzyl alcohol was received from Sinphar Chemical Reagent Co., China and used as received. Degussa-P25  $\text{TiO}_2$  was produced by Degussa Co., Ltd. All other chemicals in this work were analytical grade and used without further purification. N-doped  $\text{TiO}_2$  photocatalyst was prepared as described in previous work [33]. Preparation of the vanadyl oxalate precursor was achieved according to a typical procedure [34].

### 2.2 Photocatalyst preparation

The  $\text{Ag}_2\text{V}_4\text{O}_{11}$  microfiber with nanoprotuberances was assembled using a simple hydrothermal method. In a typical procedure, (0.4 g,  $7.38 \times 10^{-4}$  mol) vanadium oxalate ( $\text{VO}_2\text{C}_2\text{O}_4$ ) was dissolved in 20 mL water containing 2 mL of 1 M  $\text{HNO}_3$  under vigorous stirring for several minute, then (0.2 g,  $1.17 \times 10^{-3}$  mol)  $\text{AgNO}_3$  was added to the solution under continuous stirring, followed by addition of 1.5 ml of 30%  $\text{H}_2\text{O}_2$ . After 15 min, 15 mL of a benzyl alcohol was added to the solution. The obtained slightly blue translucent solution was transferred to a 40 mL Teflon-lined stainless steel autoclave. After heating in an electric oven at 210 °C for a period of 24 h, the autoclave was cooled to room temperature naturally. The final black product was separated

by centrifugation and washed with ion exchanged water ( $\rho = 18.2 \text{ M}\Omega/\text{cm}$ ) and absolute ethanol several time before drying at 50 °C overnight.

### 2.3 Characterization

The crystal structure and morphology of  $\text{Ag}_2\text{V}_4\text{O}_{11}$  was determined by X-ray powder diffractometer equipped (analysis PANalytical  $\chi$ Pert Pro, Netherlands) with CuK $\alpha$  radiation ( $k = 1.5418 \text{ \AA}$ ) at a scanning rate of  $0.02^\circ \text{ s}^{-1}$  in a  $2\theta$  range of  $10^\circ$ – $75^\circ$ , FEI Sirion 200 field emission scanning electron microscope (FESEM) and transmission electron microscope (TEM, Tecnai G220). The electron diffraction (SAED) patterns and high-resolution transmission electron microscopy (HRTEM) images were recorded on a JEM-2010FEF TEM at an acceleration voltage of 200 kV. The chemical state and compositions of products were analyzed using energy-dispersive X-ray fluorescence spectroscopy (EDXS) (EDAX Inc. EAGLE III energy-dispersive X-ray fluorescence spectroscopy). X-ray photoelectron spectrometer (XPS -AXIS-ULTRA DLD high-performance imaging, Shimadzu, Japan) were used to analyze the functional groups on surface and the chemical composition of these materials. The XPS spectrum were standardized against the contaminated carbon using referenced C 1s peak 285.0 eV. Electrospray ionization mass spectrometry (ESI-MS, Varian 310-MS), in positive ion mode. Liquid sample were introduced into the ESI by using a syringe pump and  $\text{N}_2$  flow was maintained at  $20 \text{ mL min}^{-1}$ . UV–Vis spectrophotometer (Shimadzu, Model No. 2450) was used to study the Optical properties. All the measurements were carried out at room temperature. Brunauer–Emmett–Teller (BET) surface areas were determined on a Micromeritics ASAP2020M Surface Area and Porosity Analyzer. The sample was degassed at 110 °C for 8 h under vacuum ( $10^{-5}$  bars).

### 2.4 Photocatalytic activity measurements

Taking into account that the organic pollutants become a high adsorption on the photocatalyst surface below a 80 °C [35], photocatalytic degradation of methylene blue (MB), rhodamine blue (RhB) and methyl orange (MO) dyes was carried out with 0.05 g. For dyes degradation, 11 mg of every dye powders in 1000 mL of distilled water. The as-prepared catalyst suspended in 200 mL of MB dye solution in a 250 mL three neck glass reactor equipped with a reflux condenser at 55 °C under air bubbling, magnetic stirring, visible light and pH equal to 7. Before light irradiation, the mixture was kept in the dark for 30 min with stirring to reach the adsorption–desorption equilibrium. The optical system for detecting the catalytic reaction included a 250 W mercury lamp (GYZ 220–230 V), Philips Electronics, which was placed about 15 cm above of a reaction vessel, with a

UV cut-off filter (providing visible light with  $\lambda \geq 400$  nm). The average light intensity striking the reaction solution is about  $0.8846 \text{ mW/cm}^2$ . At the given time interval, the sample was taken from the suspension and immediately centrifuged at 10,000 rpm for 1 min. The temperature during irradiation was controlled by means of a water bath. The concentration analysis of the dye was determined directly using a UV–Vis spectrophotometer (Shimadzu, model No. 2450). Kinetic analysis of degradation in different reaction systems is recorded according to a pseudo-first-order law; the corresponding formula is  $\ln C_0/C = kt$ , where  $k$  is the rate constant;  $C_0$  and  $C$  denote the main absorption peak intensities of MB at ( $\lambda_{\text{max}} = 664$  nm), RhB ( $\lambda_{\text{max}} = 553$  nm) and MO ( $\lambda_{\text{max}} = 507$  nm) before and after irradiation. The degradability of MB is represented by  $C/C_0$ . Also, the temperature effect was studied using  $\ln k = \ln A - E_a/RT$ , where  $E_a$  is the activation energy,  $A$  is the frequency factor and  $R$  is gas constant ( $R = 8.314 \text{ JK}^{-1} \text{ mol}^{-1}$ ).

### 3 Results and discussion

#### 3.1 XRD, XPS analysis

Figure 1a shows a phase composition and comparison of the XRD patterns of as-prepared  $\text{Ag}_2\text{V}_4\text{O}_{11}$  before and after the photocatalytic reaction. All diffraction peaks in Fig. 1a(I)

are identified as a monoclinic structured  $\text{Ag}_2\text{V}_4\text{O}_{11}$ , in good agreement with those in the JCPDS Card (No. 49-0166) (Fig. 1a(III)). There is a obvious change of diffraction peaks in Fig. 1a(II) after the three times photocatalytic MB degradation reaction, compared with Fig. 1a(I), indicating that the phase of the  $\text{Ag}_2\text{V}_4\text{O}_{11}$  catalyst is not stable for the present photocatalytic reaction process. X-ray photoelectron spectroscopy (XPS) analysis was employed to obtain further information about the elemental composition as sample before and a after three photoreaction cycles. The wide-scan XPS spectrum of the as catalyst Fig. 1b(I,II) reveals only presence of Ag, V and O, indicating of its high purity. The two strong peaks in Fig. 1c(I,II) at the Ag region of 367.3 and 373.7 eV are, respectively, attributed to Ag 3d 5/2 and Ag 3d 3/2, whereas the three peaks positioned at binding energy 517.6, 525.2 and 532.0 eV assigned to V 2p3/2, V2p 1/2, and O1s, respectively Fig. 1d(I,II). The decrease or boarding in the binding energy of the core level (chemical shift) usually indicates a decrease in the positive charge of the  $\text{V}^{5+}$  and  $\text{V}^{4+}$  or between  $\text{V}^{4+}$  and  $\text{V}^{3+}$  [28] which may be deformed the crystal structure of  $\text{Ag}_2\text{V}_4\text{O}_{11}$  after the three time photocatalytic process.

#### 3.2 Morphology analysis

Typical FE-SEM images with different magnification of the sample synthesized by hydrothermal process are shown in

**Fig. 1**  $\text{Ag}_2\text{V}_4\text{O}_{11}$  before and after three time photocatalytic of MB degradation **a** X-ray diffraction patterns, **b** XPS survey spectrum, **c**, **d** Ag and V high XPS resolution spectra

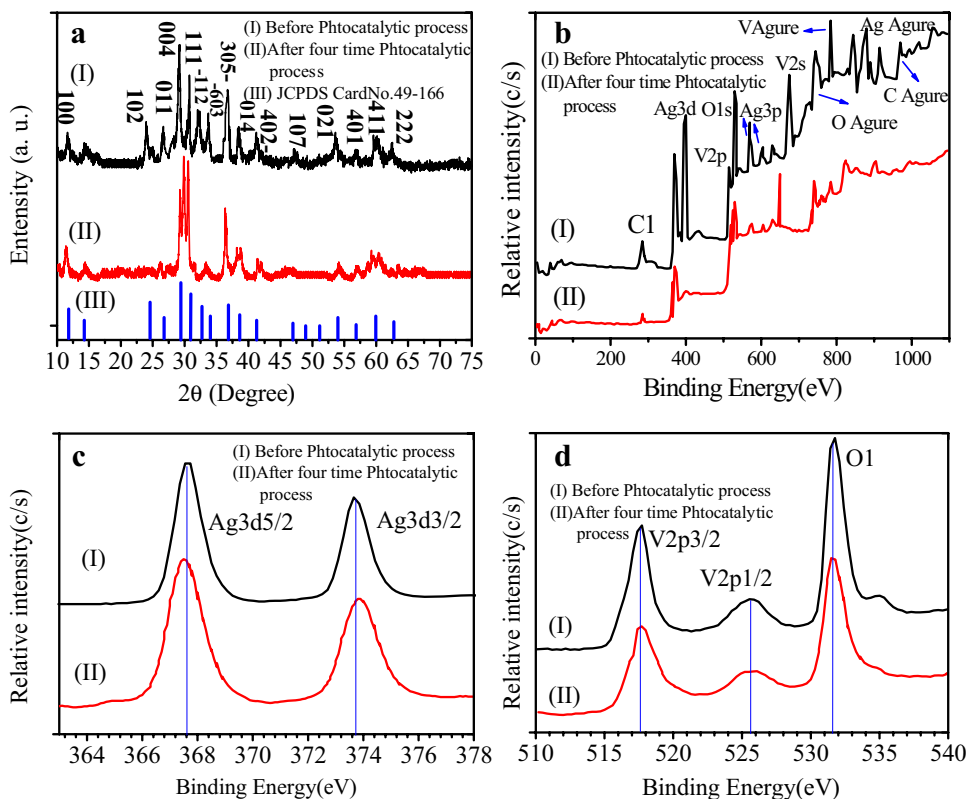
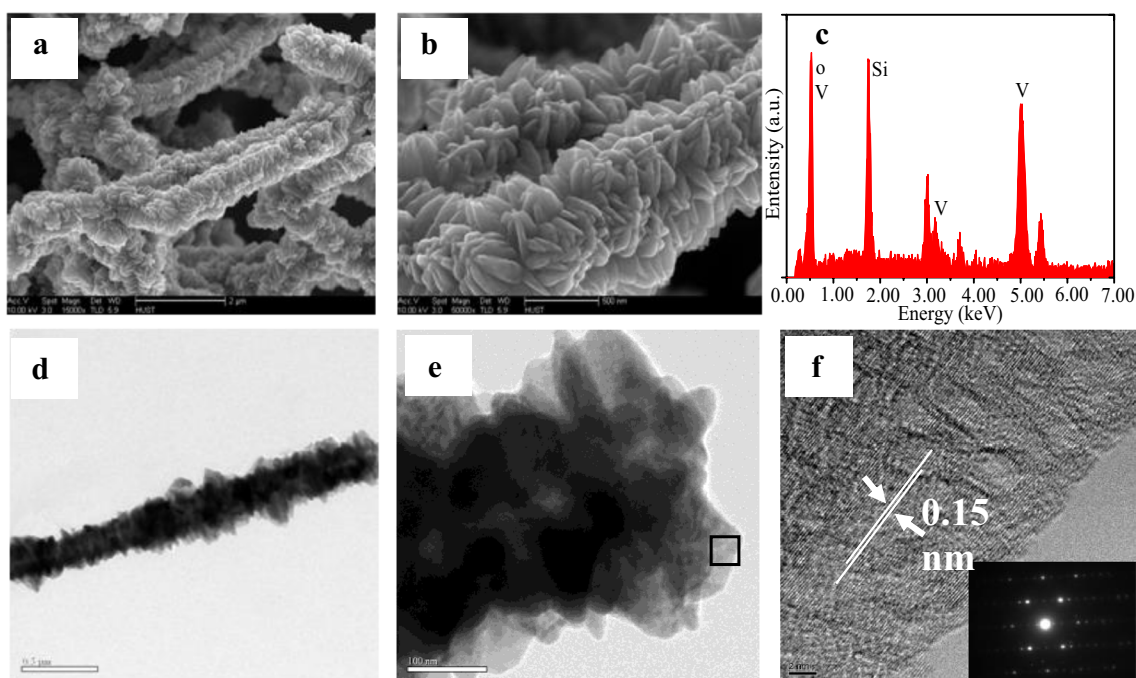


Fig. 2. Clearly, we can see that regular and uniform microfibres are close to one micrometer in diameter and several micrometers in length in Fig. 2a. High-magnification FE-SEM images in Fig. 2b reveal that the fibre surface is densely textured with protuberances of 39–60 nm thickness and 150 nm length; those protuberances vertically stand on the micro-fibre and there are gaps existing among the vertically aligned protuberances crystal. An interesting observation is the aggregate of protuberances on the surface as groups. Moreover, the corresponding EDS pattern Fig. 2c indicates that the synthesized product is composed of Ag, V, O elements (Si is from the glass grid where the sample was deposited). Further structural characterization of the  $\text{Ag}_2\text{V}_4\text{O}_{11}$  microstructures was conducted by using transmission electron microscope TEM and High resolution transmission electron microscope (HRTEM). Figure 2d shows a typical TEM image of an individual  $\text{Ag}_2\text{V}_4\text{O}_{11}$  fibre-like structure, and clearly demonstrates that the obtained  $\text{Ag}_2\text{V}_4\text{O}_{11}$  is built by large number of spherical protuberances, which gives an aspect surface area. The selected-area electron diffraction (SAED) pattern taken from an individual protuberance clearly reveals that the protuberance is a single crystal (inset in Fig. 2f). The corresponding HRTEM image at the area marked with a black rectangle in Fig. 2e of an individual  $\text{Ag}_2\text{V}_4\text{O}_{11}$  nanoprotuberance is shown in Fig. 2f, which further supports the claim of crystallinity for  $\text{Ag}_2\text{V}_4\text{O}_{11}$  protuberances microstructures. The calculated

space of the lattice fringes is 0.15 nm, which is close to the (110) plane of  $\text{Ag}_2\text{V}_4\text{O}_{11}$  crystal.

### 3.3 Effect of $\text{AgNO}_3$ , $\text{HNO}_3$ , and $\text{H}_2\text{O}_2$

Effect of Ag concentration on the morphology of as prepared microfibers was investigated under the same other conditions and the morphological features of the products were characterized by FE-SEM and X-ray diffraction. In the first, when the reaction was carried out without silver nitrate,  $\text{HNO}_3$  and  $\text{H}_2\text{O}_2$ , the product was  $\text{VO}_2$  (B) superstructure (see details in Supplementary Information SI). Then, the reaction system was consisted of  $\text{HNO}_3$ ,  $\text{H}_2\text{O}_2$  without adding  $\text{AgNO}_3$ , The scanning electron microscope FE-SEM images exhibit an agglomeration of shorts and smooth nanobelt as is shown in Fig. 3a. The X-ray diffraction spectrum Fig. 3b indicate that the product is a Shcherbiantite phase of  $\text{V}_2\text{O}_5$  with  $a = 11.50300 \text{ \AA}$ ,  $b = 0.369 \text{ \AA}$ ,  $b = 4.369 \text{ \AA}$  and  $c = 3.557 \text{ \AA}$ , which is in agreement with the standard data from JCPDS Card (No. 861-2248). Moreover, if a concentration of  $\text{AgNO}_3$  increased to  $(5.8 \times 10^{-4} \text{ mol, } 0.1 \text{ g})$  in present of  $\text{HNO}_3$  FESEM image Fig. 3c appears that the exterior surface of microfibers is composed of nanoparticles, indicating the crucial role of Ag to generation microfibers morphology. All X-ray diffraction peaks Fig. 3c can be indexed to monoclinic  $\text{Ag}_2\text{V}_4\text{O}_{11}$  which is consistent with the values given

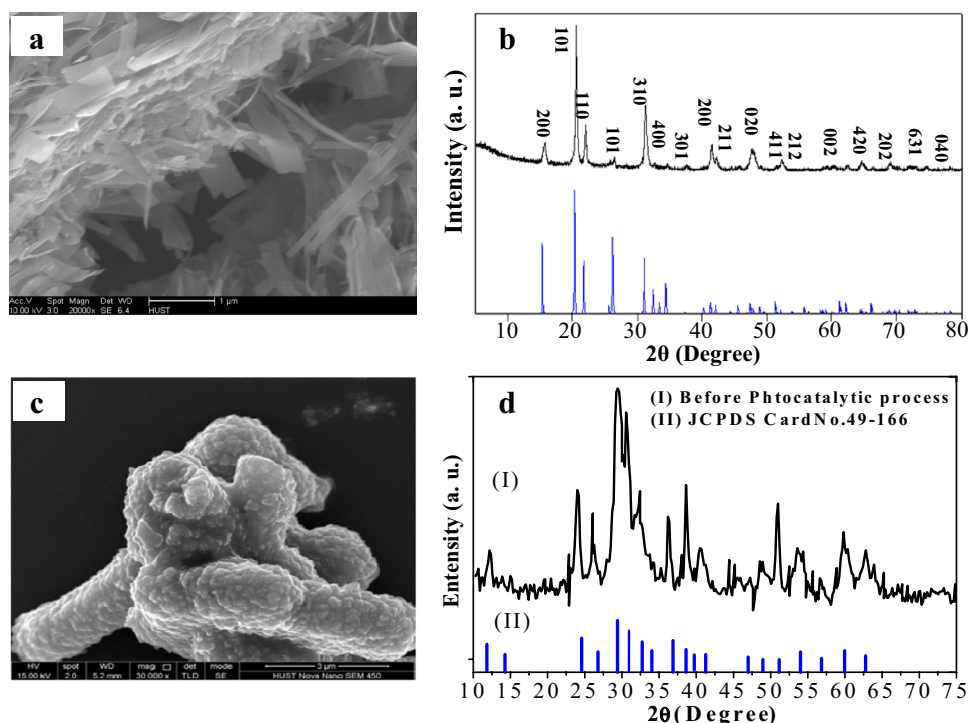


**Fig. 2** a Low and b high-magnification FE-SEM images of  $\text{Ag}_2\text{V}_4\text{O}_{11}$  micro-fibre, c energy-dispersive X-ray analysis of the  $\text{Ag}_2\text{V}_4\text{O}_{11}$  sample, d, e TEM image of single end micro-fibre, and f HRTEM image

of the protuberances like structure with selective area electron diffraction (SAED) pattern inserted



**Fig. 3** FSEM image and XRD of obtained products fabricated by a hydrothermal process at 210 °C for 24 and presents  $\text{HNO}_3$  and  $\text{H}_2\text{O}_2$ ; **a, b** without Ag; **c, d** when the dosage of  $\text{AgNO}_3$  was (0.1 g)



by JCPDS card No. 49-0166. No peaks from other phases can be detected, indicating the high purity of the sample.

### 3.4 Growth process

The formation process of hierarchical  $\text{Ag}_2\text{V}_4\text{O}_{11}$  architectures was investigated by taking out the product at various

hydrothermal treatment times of 4, 8, 12, 18, 20 and 24 h at 210 °C under the same other conditions Fig. 4. At the early stage of the hydrothermal reaction (4 h) small amorphous nanoparticles were quickly formed. When the reaction time was extended to 8 h, the tiny nanoparticles started to assemble in a certain area. After 12 h the formed nanoparticles were randomly contacted and oriented, began to form

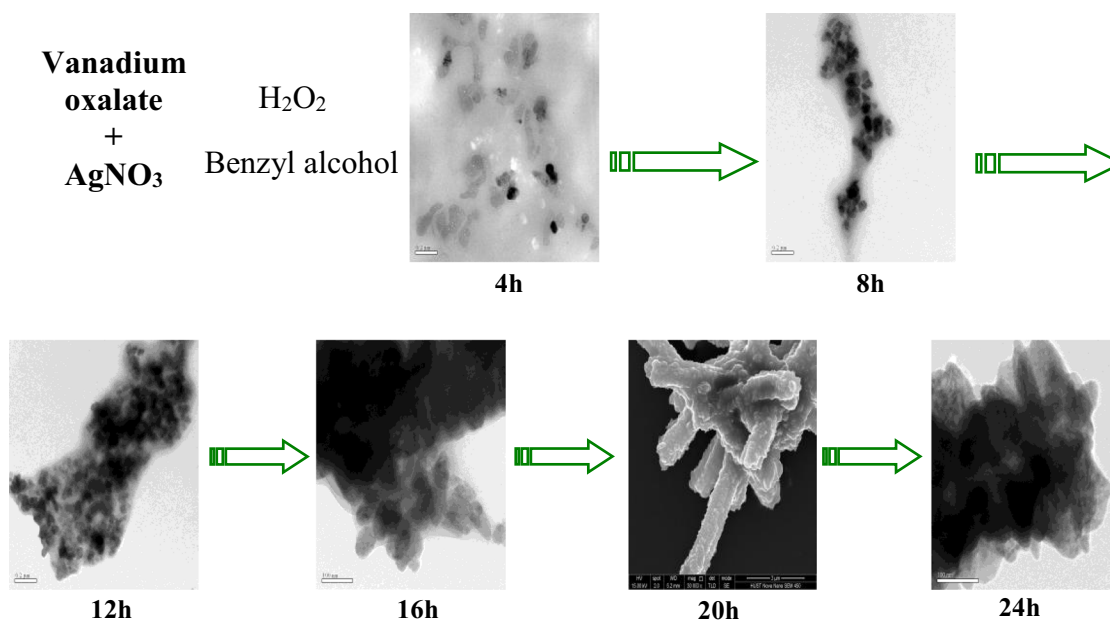


**Fig. 4** Schematic illustration of the formation process of  $\text{Ag}_2\text{V}_4\text{O}_{11}$  microfibers at 210 °C

microfiber like structures. Then, these connected nanoparticles evolved into branched microfibers with nearly similar in diameter. After 20 h hydrothermal reaction, the immature nanoprotuberances has appeared on the as prepared microfibers surface. Finally, the complete microfiber-like superstructure composed of nanoprotuberances was obtained when the reaction time was prolonged to 24 h.

It is well known that vanadium oxalate  $\text{VOC}_2\text{O}_4$  give CO and  $\text{CO}_2$  when treated thermally [36]. Generally,  $\text{AgNO}_3$  has a tendency to react with  $\text{H}_2\text{O}_2$  to form Ag and  $\text{Ag}_2\text{O}_2$ . Since the vanadium (4+) exists in  $\text{VOC}_2\text{O}_4$  with weak reducibility, we propose that the  $\text{HNO}_3$  and benzyl alcohol played an important role in the formation of vanadium (5+).  $\text{V}_2\text{O}_5$  at the presence of  $\text{HNO}_3$  leading to  $[\text{H}_2\text{V}_{10}\text{O}_{28}]^{4-}$  ions and quadruple strings structure  $[\text{V}_4\text{O}_{12}]^{4-}$  when the temperature was more increased [37]. These quadruple are further linked through sharing the edges or the corners to form a  $[\text{V}_4\text{O}_{11}]^{2-}$  layer framework structure [38, 39]. Subsequently, silver ions could accommodate with these framework tunnels to produce silver vanadium microfibers.

### 3.5 UV–Vis DRS analysis

Figure 5a, b shows the UV–Vis diffuse reflectance spectrum of the as-prepared sample. One can see that the  $\text{Ag}_2\text{V}_4\text{O}_{11}$  has an absorption edge up to about 600 nm, which covers the region from strong visible light ranges in the sunlight to

UV. Since the optical band gap  $[E_g(\text{eV})]$  of a semiconductor could be deduced according to the following equation  $\alpha h\nu = A(h\nu - E_g)^{1/2}$  [40], where  $\alpha$ ,  $h$ ,  $\nu$ ,  $E_g$ , and  $A$  are absorption coefficient, Planck constant, light frequency, band gap, and a constant, respectively, the band gap energy is obtained from the intercept of the tangent line in the plot of Abs. versus wavelength (Fig. 5b) and the value is determined to be 1.93 eV. The comparison between UV–Vis diffuse of an as-prepared sample at a reaction time of 24 and 20 h in (Fig. SII Supplementary Information). Meanwhile, valence band (VB) and conduction band (CB) positions are calculated using the theoretical prediction formula  $E_{\text{CB}} = E_{\text{VB}} - E_g$  and  $E_{\text{VB}} = X - E_C + 0.5E_g$ , where  $E_{\text{CB}}$ ,  $E_g$ ,  $E_{\text{VB}}$ ,  $E_C$  and  $X$  are the valence band (CB) edge potential energy, the band gap energy of the semiconductor, the conduction band (VB) edge potential energy, free electrons on the hydrogen scale ( $\sim 4.5$  eV) and the absolute electronegativity (5.4 eV) according to the literature [32], respectively. Therefore the value of conduction band (CB) and valence band (VB).

### 3.6 Photocatalysis performance

Firstly, the wavelength dependence of the catalytic process is generally applied to identify whether the reaction is driven by light [41, 42]. Figure 6a presents the variation of UV–Vis absorption spectra of MB solution before and after irradiation of the  $\text{Ag}_2\text{V}_4\text{O}_{11}$  at different time points. Before

**Fig. 5** UV–Vis diffuse reflectance spectrum of as prepared  $\text{Ag}_2\text{V}_4\text{O}_{11}$

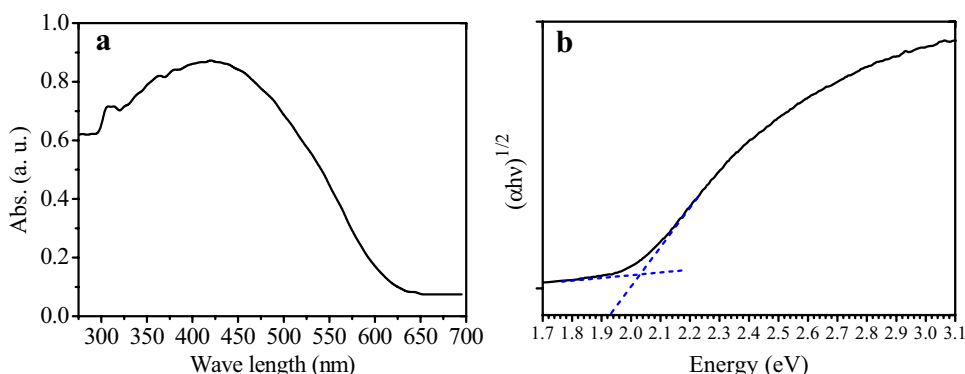
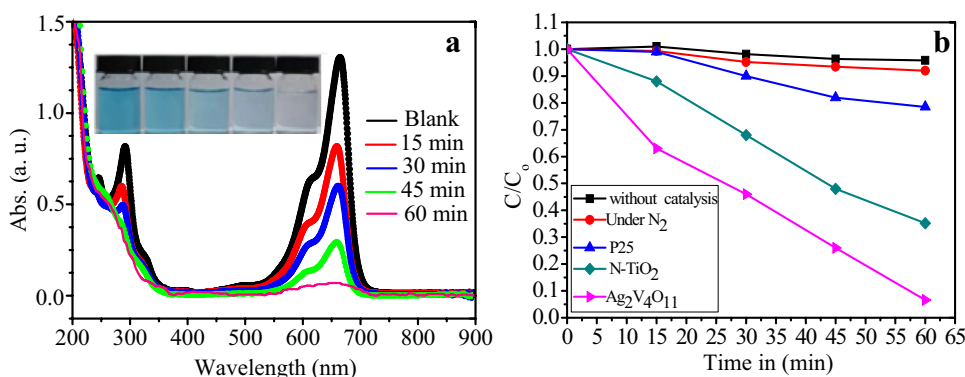


**Fig. 6** **a** UV–Vis spectra of degradation products of MB in aqueous solution with  $\text{O}_2$  and under light irradiation catalyzed by  $\text{Ag}_2\text{V}_4\text{O}_{11}$  microfibers in different times; **b** comparison of the MB decomposition with times catalyzed by  $\text{Ag}_2\text{V}_4\text{O}_{11}$  microfibers, N-TiO<sub>2</sub>, Degussa-P25 TiO<sub>2</sub> and without catalyst



exposure, there is one distinctive absorption peak in a visible region ( $\lambda_{\text{max}} = 664 \text{ nm}$ ) and two weak bands in the UV region (300–240 nm). When MB solution was treated with  $\text{O}_2$  (by pumping air) and  $\text{Ag}_2\text{V}_4\text{O}_{11}$  under visible light at pH 7 and  $55^\circ\text{C}$ , the intensities of all absorption bands were decreased with time. Also, the main absorption bands are not shifting with time, which proposes heterocyclic/benzene rings are decomposed rather than the simple decolouration of organic-groups [43]. In order to compare the photocatalytic activities of the as-prepared product, a dynamic curve of the MB degradation catalyzed by  $\text{Ag}_2\text{V}_4\text{O}_{11}$ , N-TiO<sub>2</sub> [34] and Degussa-P25 TiO<sub>2</sub> as a function of time was illustrated in Fig. 6b. The result shows 95.11, 64.81 and 21.77% MB could be removed after exposure of 60 min in the presence of  $\text{Ag}_2\text{V}_4\text{O}_{11}$  N-TiO<sub>2</sub> and Degussa-P25 respectively, despite that nano-TiO<sub>2</sub> is an efficient photocatalyst under ultraviolet light irradiation. The colour of MB stilled almost constant over 60 min with no addition of catalyst (Fig. 6b), or with no visible light irradiation or  $\text{O}_2$ , implying that the degradation of MB in this system is a photocatalytic oxidation process. The difference in efficiency could be due to the more selectivity of as product to the cationic dyes MB and RhB than anionic dye MO. The efficiency of the  $\text{Ag}_2\text{V}_4\text{O}_{11}$  as a catalyst of the degradation of two other dyes, RhB and MO, was investigated at the same condition (see Supplementary Information III). Photo activities of as sample prepared at various time and same of other reaction condition were compared (see Supplementary IV).

### 3.7 Photocatalytic mechanism

Generally, the activated species in the photooxidation process of dyes are include photogenerated holes, hydroxyl radicals  $\cdot\text{OH}$  and superoxide radicals  $\cdot\text{O}_2^-$ , while dimethyl sulfoxide (DMSO) [44, 45] and benzoquinone (BQ) [46, 47] are famous effective scavengers for  $\cdot\text{OH}$  and  $\cdot\text{O}_2^-$  radicals, respectively. Therefore, in order to get dominant active species and reveal of photoreaction mechanism of dyes over  $\text{Ag}_2\text{V}_4\text{O}_{11}$ , experiments were carried out by using of DMSO and BQ scavengers. From the Fig. 7a, b showed the dynamic

curves of MB and RhB degradation over  $\text{Ag}_2\text{V}_4\text{O}_{11}$  under the visible-light, it is easy to notice that both of trapping agents findings in, to some extent, hindered of the degradation rate of them, which indicates that  $\cdot\text{OH}$  and  $\cdot\text{O}_2^-$  radical trapping radicals as oxidation sources created on the surface of  $\text{Ag}_2\text{V}_4\text{O}_{11}$ . From Fig. 7a(I), the MB degradation efficiency was decreased significantly from 95.11 to 30.88% when the photoreaction compared with the absence of radicals scavengers in Fig. 7a(III). This added BQ as  $\cdot\text{O}_2^-$  radicals concludes that the  $\cdot\text{O}_2^-$  radicals are dominant factors in photooxidation process of MB trapping agents into, and corresponding  $\cdot\text{OH}$  and photogenerated holes radicals are inappreciable. Moreover, the  $\cdot\text{OH}$  radicals almost are not generated through the reaction between water and/or hydroxyl ion and photogenerated holes in the solutions. In contrast, the MB degradation efficiency is remained reach up to 75.18% when DMSO trapping for  $\cdot\text{OH}$  radicals add in the reaction systems Fig. 7a(II). It reveals that  $\cdot\text{O}_2^-$  radical play a significant role than  $\cdot\text{OH}$  in photooxidation process of MB due to the unimportant oxidation effect of holes, and also indicates only little amounts of  $\cdot\text{OH}$  radicals are formed by reacting of  $\cdot\text{O}_2^-$  radicals with  $\text{H}^+$  ions and photogenerated electrons in solutions. So, we believe that the main process for the photodegradation of MB is oxidation of  $\cdot\text{O}_2^-$  radicals. Taking the same ways, Fig. 7a(I) shows that the degradation efficiency of RhB solutions including BQ like as that of solutions including DMSO in Fig. 7b(II), which remain reaches near to 46.66% compared to that with no scavengers in Fig. 7b(III). It proves photogenerated holes are only a little quantity degradation of RhB, and crucial for  $\cdot\text{O}_2^-$  radicals produce and completely convert into  $\cdot\text{OH}^-$  radicals. This leads to conclude that the major method of the RhB degradation is oxidation of  $\cdot\text{O}_2^-$  radicals. Further observation Table 1, the conduction band (CB) position of  $\text{Ag}_2\text{V}_4\text{O}_{11}$  is more negative than the standard redox potential of  $\text{E}^\circ (\text{O}_2/\text{O}_2^-) = -0.33 \text{ V}$  (vs. NHE, pH 7), suggesting the photoinduced electrons on  $\text{Ag}_2\text{V}_4\text{O}_{11}$  can oxidize  $\text{O}_2$  or  $\text{H}_2\text{O}$  to form  $\text{O}_2^-$ , which is then involved in the oxidation of MB and RhB dyes. While the photoinduced holes cannot react with  $\text{OH}^-$  or  $\text{H}_2\text{O}$  to form  $\cdot\text{OH}$  because the valence band (VB)

**Fig. 7** Dynamic curves of **a, b** of MB and RhB degradation over  $\text{Ag}_2\text{V}_4\text{O}_{11}$  microfibers added radical scavengers under the visible-light with  $\lambda \geq 400 \text{ nm}$  (I added 3 ml DMSO, II added  $10^{-4} \text{ mol L}^{-1}$  BQ, III without radical scavenger)

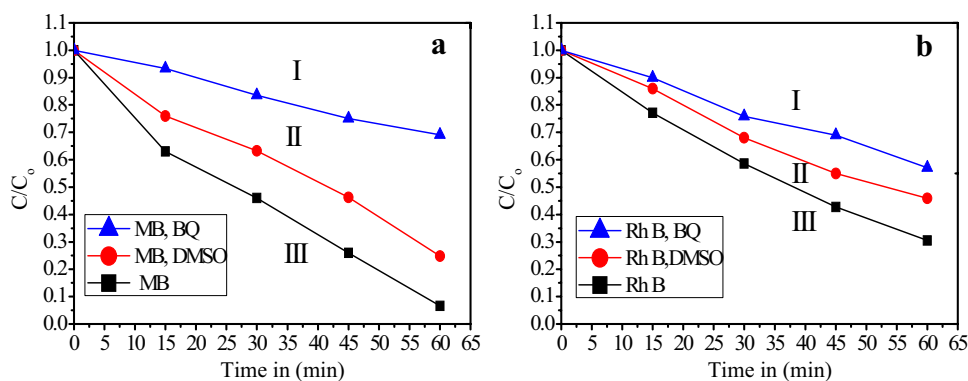


**Table 1** Optical parameters for the as  $\text{Ag}_2\text{V}_4\text{O}_{11}$  microfiber at 24 and 20 h reaction time

Time in (h)	$E_g$	$E_{\text{VB}}$	$E_{\text{CB}}$
24 h	1.93	1.865	-0.065
20 h	1.98	1.881	-0.099

position is less positive than the standard redox potential of  $E^\circ(\text{OH}/\text{OH}^-) = 1.99 \text{ V}$  (vs. NHE, pH 7). The photo-oxidation of the MB dye molecules catalyzed by the  $\text{Ag}_2\text{V}_4\text{O}_{11}$  microfibers was confirmed by (ESI-MS) electrospray ionization mass spectrometry. The ESI-MS spectrum for standard solution of MB dye (see Fig. V Supplementary Information) exhibited a strong peak at a mass/charge ( $m/z$ ) ratio of 282, which attributed to the MB dye structure without oxidation. After 60 min of visible light irradiation in the presence of the  $\text{Ag}_2\text{V}_4\text{O}_{11}$  photocatalyst, the mass spectrum for the MB dye (Fig. V Supplementary Information) displayed several signals at  $m/z = 357, 332, 318, 305, 286, 271, 254, 243, 163,$  and  $142$ . Furthermore, the lower intensity of the peak at  $m/z = 282$  compare with the spectrum of pure MB dye, indicate the formation of other species are directly proportional to the decrease of MB dye. The signals at  $m/z = 318, 357$  reflected successive superoxide radicals attack and open aromatic ring of the MB molecule, confirming that the superoxide radical played an important role in the MB dye photodegradation reaction, under the conditions used. The signals at  $m/z = 271, 254,$  and  $243$  reflected the remove one or more methyl substituents from the amine groups of

MB dye, forming the azure B, azure A, and azure C species, respectively [40]. Additionally, peaks at  $m/z = 142$  and  $162$  corresponded to cleavage of the aromatic ring resulting from attack by superoxide radical that were photogenerated in the presence of  $\text{Ag}_2\text{V}_4\text{O}_{11}$  sample under visible light irradiation. Based on the ESI-MS results, a schematic diagram (Fig. VI Supplementary Information) was proposed to clearly describe two different way simultaneously mechanism of the MB dye photodegradation catalyzed by the as-synthesized  $\text{Ag}_2\text{V}_4\text{O}_{11}$  samples. Therefore, cognition about band potential and ESI-MS spectrum will help in understanding the essential processes for photocatalytic oxidation of MB dye. Schema in (Fig. VI Supplementary Information) is demonstrated: (i) photoexcitation of electrons from the conduction band (CB); (ii) the CB electrons and a little holes of VB will react with the adsorbed  $\text{O}_2, \text{OH}^-$  and  $\text{H}_2\text{O}$ , producing  $\text{O}_2^{\cdot-}$  radicals and  $\text{H}_2\text{O}_2$ , respectively; (3) these oxidation species,  $\text{H}_2\text{O}_2$  and  $\text{O}_2^{\cdot-}$ , will oxidize the organic dyes.

### 3.8 Kinetics

To obtain more information about the photoreaction between the  $\text{Ag}_2\text{V}_4\text{O}_{11}$  microfibers and MB dye. Since the irradiation light is constant and oxygen is excessive to reducing the recombination of photogenerated surface electrons with holes, the reaction rate is only reliant on the concentration of MB, the rate constant  $k$  ( $\text{min}^{-1}$ ) was calculated by Langmuir–Hinshelwood (L–H) first-order kinetic. Figure 8a, rate constant  $k$  can be given by the slope of fitting curves, when plotting  $\ln(C/C_0)$  against time. The

**Fig. 8** **a** Kinetics of the MB degradation catalyzed by  $\text{Ag}_2\text{V}_4\text{O}_{11}$  microfibers, N-TiO<sub>2</sub>, Degussa-P25 and TiO<sub>2</sub> at 55 °C, **b** kinetics of the MB degradation catalyzed by microfibers fabricated at 20 and 24 h reaction time at 55 °C, **c** effects temperature on the decomposition of MB between microfibers by  $\text{Ag}_2\text{V}_4\text{O}_{11}$  fabricated at 20 and 24 h reaction time at 55 °C

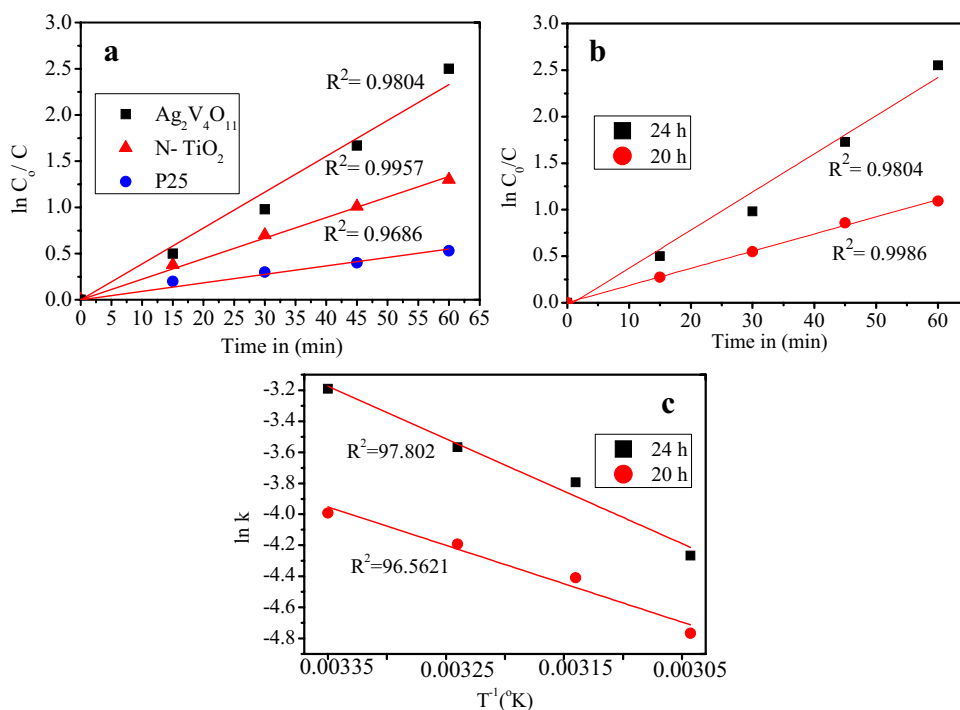
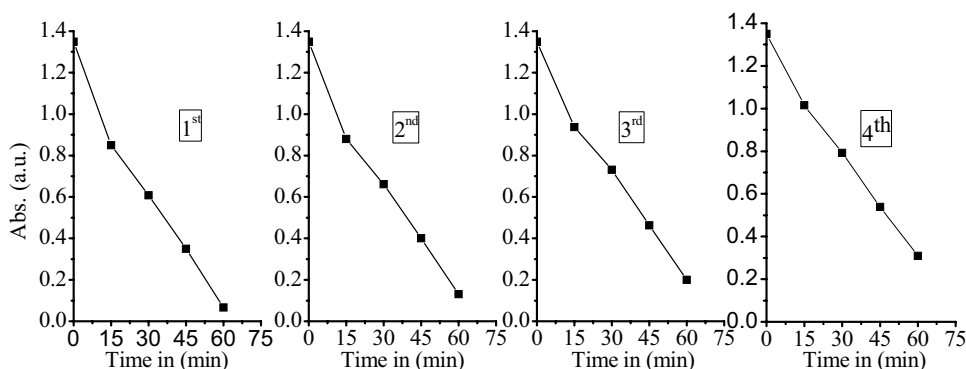




**Fig. 9** Reusability of  $\text{Ag}_2\text{V}_4\text{O}_{11}$  microfiber prepared at 24 h reaction time as the catalyst of the photocatalytic degradation of MB dye in terms of normalized values of concentration versus time showing four rounds 1, 2, 3, and 4 of degradation experiments under visible-light irradiation



apparent degradation rate constant of MB in the presence of  $\text{Ag}_2\text{V}_4\text{O}_{11}$  microfibers, N-TiO<sub>2</sub> and commercial photocatalyst P25 are  $4.11 \times 10^{-1} \text{ min}^{-1}$ ,  $2.15 \times 10^{-1} \text{ min}^{-1}$ , and  $0.787 \times 10^{-1} \text{ min}^{-1}$ , respectively. The results evaluate that the  $\text{Ag}_2\text{V}_4\text{O}_{11}$  to be a better photocatalyst than N-using the TiO<sub>2</sub> and P25 in the visible light irradiation. As expected, rate constant  $k$  of  $\text{Ag}_2\text{V}_4\text{O}_{11}$  nanofibers prepared at 24 h reaction time was  $4.11 \times 10^{-1} \text{ min}^{-1}$ , comparatively higher than rate constant  $k$   $1.18 \text{ min}^{-2}$  that of  $\text{Ag}_2\text{V}_4\text{O}_{11}$  microfibers prepared at 20 h Fig. 8b. The high rate constant  $k \text{ min}^{-1}$  value was attributed to increased surface area  $34 \text{ m}^2/\text{g}$  of  $\text{Ag}_2\text{V}_4\text{O}_{11}$  microfiber prepared at 24 h reaction time than  $19.56 \text{ m}^2/\text{g}$  that prepared at 20 h [48]. Generally, increasing of  $\text{Ag}_2\text{V}_4\text{O}_{11}$  microfiber surface area at 24 h reaction time resulted in a greater growth of protuberances on the microfiber surface. The comparative activation energy  $E_a$  of as prepared  $\text{Ag}_2\text{V}_4\text{O}_{11}$  microfiber at 20 and 24 h reaction time was calculated from the Arrhenius plot of  $\ln k$  versus  $1/T$  the slope of a linear plot is equal to  $-E_a/R$ . Figure 8c demonstrates activation energy ( $E_a$ ) of the reaction is decreased with the increase of preparations reaction time from  $28.589 \text{ kJ mol}^{-1}$  at 20 h to the  $20.109 \text{ kJ mol}^{-1}$  when reaction time is 24 h. The obtained activation energy is nearly high, which indicates that the photocatalytic process is temperature dependent. This performance could be described on the basis of photonic activation, in general the irradiation is the primary source of hole–electron pair generation which responsible for beginning photoreaction, so photocatalytic systems require some heating and not operate at near ambient temperature. The catalytic stability also was explored up to four successive cycles and found that the MB degradation efficiency was 95.11, 90.29, 85.18, 80.07 and 77.03% after 60 min of reaction and at  $55 \text{ }^\circ\text{C}$ , respectively. Comparison of photocatalytic performance was made between the materials developed in this work and other have similar band gap [49–54], as shown in (Table 2 Supplementary Information). The as-results liberated that the photocatalytic activity of the as-catalyst has a not slight decrease after each cycle Fig. 9. The reason partly is due to expectable loss during the recovery of

as-catalyst and immobilization, which reduces the active surface and adsorption ability [55, 56].

## 4 Conclusion

In summary,  $\text{Ag}_2\text{V}_4\text{O}_{11}$  microfiber with a densely characteristic of texture with protuberances of 39–60 nm thickness and 150 nm length has been successfully synthesized by a hydrothermal route in the present study. The effects of Ag concentration on the product morphology were investigated. The photocatalytic properties of the as-prepared hierarchical nanomaterials were comparatively evaluated with N-doped TiO<sub>2</sub> and P25 under visible-light illumination using a heteropolycyclic dye methylene blue, as the probe molecule. The main active species were determined to be superoxide radicals under visible-light irradiation through free-radical-trapping experiments. kinetics data of dyes degradation are fit well with the pseudo-first-order model. Moreover, methylene blue could be oxidized into several intermediates and these intermediates could be further decomposed into carbon dioxide and water. Considering the degradation efficiency of MB catalyzed by the  $\text{Ag}_2\text{V}_4\text{O}_{11}$  product at 24 h reaction time was about 95.11% at pH 7 and  $55 \text{ }^\circ\text{C}$  for 60 min are expected to find practical applications in environmental remediation under visible light irradiation.

## References

1. X. Chen, L. Liu, P.Y. Yu, S.S. Mao, *Science* **331**, 746–750 (2011)
2. P. Dong, Y. Wang, B. Cao, S. Xin, L. Guo, J. Zhang, F. Li, *Appl. Catal. B* **132–133**, 45–53 (2013)
3. B. Babu, M. Cho, C. Byon, J. Shim, *J. Alloys Compd.* **731**, 162–171 (2018)
4. Y. Liu, J. Kong, J. Yuan, W. Zhao, X. Zhu, C. Sun, J. Xie, *Chem. Eng. J.* **331**, 242–254 (2018)
5. S. Sakthivel, M. Janczarek, H. Kisch, *J. Phys. Chem. B* **108**, 19384–19387 (2004)
6. R. Abe, H. Takami, N. Murakami, B. Ohtani, *J. Am. Chem. Soc.* **130**, 7780–7781 (2008)

7. S.S. Soni, M.J. Henderson, J.F. Bardeau, A. Gibaud, *Adv. Mater.* **20**, 1493–1498 (2008)
8. L. Gomathi Devi, R. Kavitha, *RSC Adv.* **4**, 28265–28299 (2014)
9. M. Wang, J. Ioccozia, L. Sun, C. Lin, Z. Lin, *Energy Environ. Sci.* **7**, 2182–2202 (2014)
10. J.M. Wu, *J. Phys. Chem. C* **119**, 1433–1441 (2015)
11. R.G. Chaudhuri, S. Paria, *Dalton Trans.* **43**, 5526–5534 (2014)
12. X. An, X. Yu, J.C. Yu, G. Zhang, *J. Mater. Chem. A* **1**, 5158–5164 (2013)
13. W. Wang, M.O. Tadó, Z. Shao, *Prog. Mater. Sci.* **92**, 33–63 (2018)
14. J. Xiong, G. Cheng, F. Qin, R. Wang, H. Sun, R. Chen, *Chem. Eng. J.* **220**, 228–236 (2013)
15. T. Yang, J. Peng, Y. Zheng, X. He, Y. Hou, L. Wu, X. Fu, *Appl. Catal. B* **221**, 223–234 (2018)
16. A. Di Paola, E. García-López, G. Marci, L. Palmisano, *J. Hazard. Mater.* **211–212**, 3–29 (2012)
17. T. Kako, N. Kikugawa, J. Ye, *Catal. Today* **131**, 197–202 (2008)
18. S. Ouyang, N.K.D. Chen, Z. Zou, J. Ye, *J. Phys. Chem. C* **113**, 1560–1566 (2009)
19. H. Dong, Z. Li, X. Xu, Z. Ding, L. Wu, X. Wang, X. Fu, *Appl. Catal. B* **89**, 551–556 (2009)
20. Z. Yi, J. Ye, N. Kikugawa, T. Kako, S. Ouyang, H. Stuart-Williams, H. Yang, J. Cao, W. Luo, Z. Li, *Nat. Mater.* **9**, 559–564 (2010)
21. Y. Bi, S. Ouyang, N. Umezawa, J. Cao, J. Ye, *J. Am. Chem. Soc.* **133**, 6490–6492 (2011)
22. S.Y. Song, Y. Zhang, Y. Xing, C. Wang, J. Feng, W.D. Shi, G.L. Zheng, H.J. Zhang, *Adv. Funct. Mater.* **18**, 2328–2334 (2008)
23. M. Feng, M. Zhang, J.M. Song, X.G. Li, S.H. Yu, *ACS Nano* **5**, 6726–6735 (2011)
24. X.X. Liu, C. Qin, L. Cao, Y. Feng, Y. Huang, L. Qin, H.J. Seo, *J. Alloys Compd.* **724**, 381–388 (2017)
25. H. Kato, H. Kobayashi, A. Kudo, *J. Phys. Chem. B* **106**, 12441–12447 (2002)
26. P.Y. Zavalij, M.S. Whittingham, *Acta Crystallogr. Sect. B* **55**, 627–663 (1999)
27. Z. Shaoyan, L. Min, *Adv. Sci. Lett.* **4**, 3701–3705 (2011)
28. Y. Xu, X. Han, L. Zheng, S. Weid, Y. Xie, *Dalton Trans.* **40**, 10751–10757 (2011)
29. G. Shen, D. Chen, *J. Am. Chem. Soc.* **128**, 11762–11763 (2006)
30. S. Zhang, W. Li, C. Li, J. Chen, *J. Phys. Chem. B* **110**, 24855–24863 (2006)
31. Y. Liang, L.F. Zhu, P. Liu, H.B. Li, J. Xiao, X.W. Jib, G.W. Yang, *CrystEngComm* **15**, 6131–6135 (2013)
32. H. Shi, Z. Li, J. Kou, J. Ye, Z. Zou, *J. Phys. Chem. C* **115**, 145–151 (2011)
33. P. Ju, H. Fan, S. Ai, D. Zhang, Y. Wang, *Res. Chem. Intermed.* **41**, 3683–3697 (2015)
34. G. Yang, Z. Jiang, H. Shi, T. Xiao, Z. Yan, *J. Mater. Chem.* **20**, 5301–5309 (2010)
35. U.I. Gayaa, A.H. Abdullah, *J. Photochem. Photobiol. C* **9**, 1–12 (2008)
36. F.Y. Kong, M. Li, X.Y. Yao, J.M. Xu, A.D. Wang, Z.P. Liu, G.H. Li, *CrystEngComm* **14**, 3858–3861 (2012)
37. O. Durupthy, M. Jaber, N. Steunou, J. Maquet, G.T. Chandrappa, J. Livage, *Chem. Mater.* **17**, 6395–6402 (2005)
38. M. Onoda, K. Kanbe, *J. Phys.* **13**, 6675–6685 (2001)
39. X. Chen, X.M. Sun, Y.D. Li, *Inorg. Chem.* **41**, 4524–4530 (2002)
40. S. Xue, H. He, Z. Wu, C. Yu, Q. Fan, G. Peng, K. Yang, *J. Alloys Compd.* **694**, 989–997 (2017)
41. R. Abe, M. Higashi, K. Sayama, Y. Abe, H. Sugihara, *J. Phys. Chem. B* **110**, 2219–2226 (2006)
42. L. Yu, Y. Huang, G. Xiao, D. Li, *J. Mater. Chem. A* **1**, 9637–9640 (2013)
43. K. Zhang, X. Sun, G. Lou, X. Liu, H. Li, Z. Su, *Mater. Lett.* **59**, 2729–2731 (2005)
44. X. Yang, F. Ma, K. Li, Y. Guo, J. Hub, W. Li, M. Huo, Y. Guo, *J. Hazard. Mater.* **175**, 429–438 (2010)
45. X.X. Hu, C. Hu, *J. Solid State Chem.* **180**, 725–732 (2007)
46. N.E. Polyakov, T.V. Leshina, E.S. Meteleva, A.V. Dushkin, T.A. Konovalova, L.D. Kispert, *J. Phys. Chem.* **114**, 14200 (2010)
47. V. Brezova, M. Valko, M. Breza, H. Morris, J. Telsler, D. Dvoranova, K. Kaiserov, L. Varecka, M. Mazur, D. Leibfritz, *J. Phys. Chem. B* **107**, 2415–2425 (2003)
48. M. Styliidi, D.I. Kondarides, E.X. Verykios, *Appl. Catal. B* **47**, 189–201 (2004)
49. Z.S. Liu, B.T. Wu, Y.B. Zhu, *Mater. Chem. Phys.* **135**, 474–478 (2012)
50. H. sun, P.S. Tong, *Adv. Mater. Res.* **486**, 55–59 (2012)
51. X. Xu, C. Randorn, P. Efstathiou, J.T.S. Irvine, *Nat. Mater.* **11**, 595–598 (2012)
52. C. Belder, C. Adán, S. García-Rodríguez, M. Fernández-García, *Chem. Eng. J.* **224**, 24–31 (2013)
53. J. Gómez-Pastora, S. Dominguez, E. Bringas, M.J. Rivero, I. Ortiz, D.D. Dionysiou, *Chem. Eng. J.* **310**, 407–427 (2017)
54. W. Wang, F. Huang, X. Lin, *Scr. Mater.* **56**, 669–672 671 (2007)
55. E. Baciocchi, T.D. Giacco, F. Elisei, F.M. Gerini, M. Guerra, S. Capi, P. Liberali, *J. Am. Chem. Soc.* **125**, 16444–16454 (2003)
56. H.A. Abbood, H. Peng, X. Gao, B. Tan, K. Huang, *Chem. Eng. J.* **209**, 245–254 (2012)